Astronomy & Astrophysics manuscript no. paperSPI˙AST˙V6
January 26, 2015

The GAPS Programme with HARPS-N at TNG

VII. Putting exoplanets in the stellar context: magnetic activity and asteroseismology of τ Bootis A*

F. Borsa[1], G. Scandariato[2], M. Rainer[1], A. Bignamini[3], A. Maggio[4], E. Poretti[1], A. F. Lanza[2], M. P. Di Mauro[5], S. Benatti[6], K. Biazzo[2], A. S. Bonomo[7], M. Damasso[7], M. Esposito[8,9], R. Gratton[6], L. Affer[4], M. Barbieri[6], C. Boccato[6], R. U. Claudi[6], R. Cosentino[2,10], E. Covino[11], S. Desidera[6], A. F. M. Fiorenzano[10], D. Gandolfi[2,12], A. Harutyunyan[10], J. Maldonado[4], G. Micela[4], P. Molaro[3], E. Molinari[10,13], I. Pagano[2], I. Pillitteri[4,14], G. Piotto[6,15], E. Shkolnik[16], R. Silvotti[7], R. Smareglia[3], J. Southworth[17], A. Sozzetti[7], B. Stelzer[4]

[1] INAF – Osservatorio Astronomico di Brera, Via E. Bianchi 46, 23807 Merate (LC), Italy
[2] INAF – Osservatorio Astrofisico di Catania, Via S.Sofia 78, 95123, Catania, Italy
[3] INAF – Osservatorio Astronomico di Trieste, via Tiepolo 11, 34143 Trieste, Italy
[4] INAF – Osservatorio Astronomico di Palermo, Piazza del Parlamento, 1, 90134, Palermo, Italy
[5] INAF-IAPS Istituto di Astrofisica e Planetologia Spaziali, Via del Fosso del Cavaliere 100, 00133, Roma, Italy
[6] INAF – Osservatorio Astronomico di Padova, Vicolo dell'Osservatorio 5, 35122, Padova, Italy
[7] INAF – Osservatorio Astrofisico di Torino, Via Osservatorio 20, 10025, Pino Torinese, Italy
[8] Instituto de Astrofísica de Canarias, C/Via Láctea S/N, 38200 La Laguna, Tenerife, Spain
[9] Departamento de Astrofísica, Universidad de La Laguna, 38205 La Laguna, Tenerife, Spain
[10] Fundación Galileo Galilei - INAF, Rambla José Ana Fernandez Pérez 7, 38712 Breña Baja, TF - Spain
[11] INAF – Osservatorio Astronomico di Capodimonte, Salita Moiariello 16, 80131, Napoli, Italy
[12] Landessternwarte Königstuhl, Zentrum für Astronomie der Universitat Heidelberg, Königstuhl 12, 69117 Heidelberg, Germany
[13] INAF - IASF Milano, via Bassini 15, 20133 Milano, Italy
[14] Harvard-Smithsonian Center for Astrophysics, 60 Garden Street, Cambridge, MA, 02138, USA
[15] Dip. di Fisica e Astronomia Galileo Galilei – Università di Padova, Vicolo dell'Osservatorio 2, 35122, Padova, Italy
[16] Lowell Observatory, 1400 W. Mars Hill Road, Flagstaff, AZ, 86001, USA
[17] Astrophysics Group, Keele University, Staffordshire, ST5 5BG, UK

Received ; accepted

Abstract

Aims. In the context of the GAPS program, we observed the τ Boo system with the HARPS-N spectrograph in order to test a new observational strategy, aimed to jointly study asteroseismology, the planetary orbit and star-planet magnetic interaction.
Methods. We took high-cadence observations on 11 nearly consecutive nights, and for each night averaged the raw FITS files using a dedicated software, in order to obtain high S/N spectra and radial velocity values free from stellar oscillations, without losing this latter information. Specific software was written to build a new custom mask, used to refine the RV determination with the HARPS-N pipeline, and to perform the spectroscopic analysis.
Results. We updated the planetary ephemeris and proved the acceleration due to the stellar binary companion. The study of stellar activity variation suggests the presence of an high-latitude plage during the time span of our observations. The correlation between the chromospheric activity and the planetary orbital phase remains unclear. Solar-like oscillations are detected in the radial velocity timeseries: we could estimate asteroseismic quantities, finding a good agreement with theoretical predictions. With the stellar model built we found for τ Boo an age of 0.9 ± 0.5 Gyr, and could further constrain the value of the stellar mass to 1.38 ± 0.05 $M_\odot$.

Key words. Stars: individual: τ Boo – planetary systems – Asteroseismology – techniques: spectroscopic – Stars: activity

1. Introduction

While the number of confirmed exoplanets is rapidly increasing, we are improving the ability to characterize them, also by means of studying their parent stars and the star-planet tidal or magnetic interactions. At the moment, the most interesting targets for characterization are transiting exoplanets, but the large population of non-transiting ones solicits new methods and observation strategies for this purpose.

In our intent of characterizing planetary systems with a spectro-photometric approach, we selected the well-known system τ Bootis A (HD 120136, F6V, V=4.49) as a test case in the framework of the project Global Architecture of Planetary Systems[1] (GAPS, Covino et al. 2013). GAPS is a joint effort of Italian researchers in collaboration with a few experts abroad,

Send offprint requests to: F. Borsa
e-mail: francesco.borsa@brera.inaf.it

* Based on observations made with the Italian Telescopio Nazionale Galileo (TNG) operated on the island of La Palma by the Fundacion Galileo Galilei of the INAF at the Spanish Observatorio Roque de los Muchachos of the IAC in the frame of the program Global Architecture of the Planetary Systems (GAPS).

[1] http://www.oact.inaf.it/exoit/EXO-IT/Projects/Entries/2011/12/27_GAPS.html

and the GAPS team manages a long-term observation program with the high-precision HARPS-N spectrograph (Cosentino et al. 2012) at the Telescopio Nazionale Galileo (TNG). τ Boo A is included in the sub-program dedicated to the characterization of planetary systems through studies of their interactions with the central stars. Its brightness allows us in particular to perform high-resolution spectroscopy and asteroseismology with a limited investment of telescope time.

The bright F6V star has a faint M2V companion (separation 1.83", Drummond 2014), τ Boo B, forming a long period binary system. The primary component (hereafter τ Boo for sake of uniformity with current literature) was first claimed to host a planet with a period of 3.312 days by Butler et al. (1997), using the radial velocity method. Thanks to its brightness, this system was employed in the past to develop new analysis techniques that have been later applied to other stars. Among the most important discoveries, there are the definition of upper limits on reflected starlight providing a maximum value for the planet's albedo (Collier Cameron et al. 1999; Rodler et al. 2010), the spectroscopic detection of CO absorption lines in the planet atmosphere that permitted to determine the inclination angle of the system, and thus the exact mass of the planet (M_p=5.95 ± 0.28 M_{Jup}, Brogi et al. 2012; Rodler et al. 2012) and, very recently, the first detection of water vapor in the atmosphere of a non-transiting exoplanet (Lockwood et al. 2014).

τ Boo was also considered in searches for star-planet magnetic interaction (SPMI) effects. In fact, a peculiar characteristic of this star is the presence of an optical variable modulation of the light curve likely due to photospheric spots which persisted at fixed longitudes for a few hundred days, as observed by the MOST satellite (Walker et al. 2008). SPMI is a long debated issue, with the best evidence coming from modulation of chromospheric activity tracers phased with the planetary orbital period rather than with the stellar rotation period (Shkolnik et al. 2005, 2008; Lanza 2009, 2012).

Assessment of this behavior requires long-term monitoring of stars with close-in massive planets (hot Jupiters), very high signal–to–noise spectra (S/N> 300 at 3950Å) and adequate resolving power ($R \geq 80000$) to measure variability in the core of deep chromospheric lines such as the Ca II H&K doublet. Detecting periodicities and relating them to the planet period is crucial, because variability can be due to intrinsic stellar activity, not related to the presence of hot Jupiters. On the other hand, the study of stellar activity is important as a source of "noise" in the search and characterization of new planets in extra-solar systems.

In the case of τ Boo, previous searches for SPMI in the Ca II H&K lines were unsuccessful (Shkolnik et al. 2005). One possible reason is that SPMI is due to magnetic stresses between the stellar and planetary magnetic fields, but this effect is very limited in τ Boo because the stellar rotation is known to be synchronized with the orbital motion of the planet (e.g., Henry et al. 2000). Nonetheless, this system remains an interesting target because the parent star shows evidence of magnetic cycles, with polarity reversals happening every ~ 2 years (e.g., Catala et al. 2007; Donati et al. 2008; Fares et al. 2009).

Asteroseismology of stars hosting exoplanets received a great boost from the photometric time series collected by space missions. On the other hand, spectroscopic campaigns aimed at detecting solar-like oscillations are very hard to organize due to the long time baseline requested to resolve and identify the excited modes. For instance, Bazot et al. (2012) could obtain a measure of the large separation of 18 Sco by means of 2833 datapoints collected over 12 complete nights. It is difficult to insert an asteroseismic program in a large project as GAPS, covering a multiplicity of sub-programs and goals within such limited telescope time. Moreover, the exposure times have to be very short to monitor the solar-like oscillations and consequently the asteroseismic targets have to be bright stars. Therefore, we did not miss the opportunity offered by the scientific case of τ Boo, matching very well some exoplanetary goals (search for additional planets and study of the star-planet interaction), to use it as a pathfinder in applying the high-cadence observation strategy for asteroseismic purposes.

The paper is structured as following: Sect. 2 presents the observations and describes the data reduction. Sect. 3 is devoted to the spectral analysis, with results presented in Sect. 4 (stellar parameters), Sect. 5 (orbital parameters), Sect. 6 (stellar activity), Sect. 7 (asteroseismology) and Sect. 8 (evolutionary stage). Conclusions are presented in Sect. 9.

2. Observations and data reduction

τ Boo was observed with HARPS-N on 11 nights between April 13th and May 8th 2013, obtaining a very good phase coverage of the orbital period of the planet. A few more observations were done in April and July 2014, to characterize the long-term trend observed. Th-Ar simultaneous calibration was used to improve the radial velocity (RV) precision. The complete set of observations is shown in Table 1. When possible, right after the target we observed the telluric standard star η UMa (B3V, V=1.84, $V\sin i = 205$ km s^{-1}), thus providing a tool to remove telluric lines.

Table 1. HARPS-N RV observations of τ Boo. This table is available in its entirety online at the CDS.

BJD_{UTC}-2450000.	RV (m s^{-1})	RV err (m s^{-1})	Bis. span (m s^{-1})
6396.517465	-16145.21	0.83	-104.71
6396.518460	-16136.13	0.83	-114.74
6396.519444	-16141.63	0.84	-109.08
6396.520439	-16141.12	0.80	-102.26
...	...	...	...

In order to study the star-planet interaction, we needed to reach a high signal–to–noise ratio (S/N) in the zone of Ca II H&K lines. Unfortunately, to match this requirement with a single exposure, given the spectral energy distribution of τ Boo combined with the lower efficiency of HARPS-N in the blue region, would cause the saturation of the rest of the spectrum. We were thus able to create a synergy between two components of the GAPS campaign: for such a bright star the need to avoid saturation well integrated with the requirements of an asteroseismic feasibility study of τ Boo with HARPS-N. Our observational strategy consisted in taking several subsequent short exposure spectra (1 minute long) and then to average them to obtain a single spectrum with a very high S/N. In such a way we could obtain the high-cadence spectra to monitor the solar-like oscillations and get mean spectra to cover the orbital phase of the planet. Moreover, we also get RV values to study the long-term stability of the system.

We developed an interactive program written in Python language (Borsa et al. 2013) to average the raw images pixel by pixel, adjusting the header of the created files. The resulting mean FITS files are ready to be passed through the HARPS-N

pipeline, in order to be reduced exactly in the same way as all the FITS files acquired with HARPS-N (Table 2).

The Julian dates of the mean files calculated by the pipeline are not the correct ones due to the presence of the overhead time between the single exposures: since this time is ∼25 sec, its influence on consecutive 1 min exposures is quite relevant. We corrected for that by taking an average of the Julian dates of the single images, weighted on their respective S/N: in this way we introduced a sort of exposure-meter information on the long exposure mean file. The RVs are then corrected for the change in the Barycentric Earth Radial Velocity (BERV) between the pipeline-estimated Julian date and the corrected one. For this purpose, we created a new tool and verified it to be comparable with the HARPS-N pipeline at the level of ~ 3 cm s^{-1} in the BERV for different coordinates and dates (Borsa et al. 2013).

Table 2. RVs for the generated τ Boo mean files. ϕ refers to the orbital phase of the planetary companion, based on ephemeris of Sect. 5 and considering the planetary inferior conjunction as ϕ=0.

Night	BJD_{UTC}-2450000	RV [m s^{-1}]	RV err [m s^{-1}]	ϕ
1	6396.531788	-16135.08	0.86	0.73
2	6397.536059	-16716.81	0.77	0.03
3	6398.499820	-17016.77	0.93	0.33
4	6399.548081	-16231.25	1.39	0.65
5	6401.498724	-17085.13	0.79	0.23
6	6402.497328	-16501.11	1.31	0.53
7	6406.653040	-16169.98	0.78	0.79
8	6407.703825	-16904.41	0.89	0.10
9	6408.686713	-16878.51	0.96	0.40
10	6410.680969	-16603.65	1.34	0.00
11	6421.517542	-17054.54	0.97	0.27

The final reduction of the data (324 single exposures and 11 mean exposures) was done using the HARPS-N Data Reduction Software (DRS) pipeline on the Yabi platform. Yabi (Hunter et al. 2012) is a Python web application installed at IA2[2] in Trieste, that allows authorized users to run the HARPS-N DRS pipeline on their own proprietary data with custom input parameters.

The pipeline installed at the TNG estimates the radial velocities of the targets by computing a cross-correlation function (CCF, Pepe et al. 2002) using the best suited line mask amongst the available ones (G2, K5 or M2 spectral type). Taking advantage of the Yabi platform, we were able to create and implement a new custom mask for τ Boo (Rainer 2013; Gratton 2013). Using the standard G2 mask as a starting point, we measured the depths of several unblended lines in a well-exposed, high S/N τ Boo spectrum. From these measurements, we found the following empirical correlation between the line depths (LD) of the G2 mask and those of the τ Boo spectrum: $LD_{\tau\ Boo} = 0.0409321 \cdot e^{2.80654 \cdot LD_{G2}}$. Using this equation, we corrected the values of the line depths in the standard G2 mask and created the new custom mask (3625 photospheric lines) that we used for the data reduction. In addition to this, we increased the width of the half-window of the weighted CCF from the default value of 20 up to 30 km s^{-1}(about twice the value of Vsin *i* of the star), in order to well cover the continuum around the wings of the mean line profile. In such a way, we reduced the RV errors by ∼5%.

[2] http://ia2.oats.inaf.it/

3. Spectral Analysis

The analysis of the magnetic activity of τ Boo was performed by using the high S/N mean spectra. The CCF provided by the DRS pipeline is computed by cross-correlating the spectrum of τ Boo with the custom mask (see Sect. 2): it is thus essentially a high S/N mean line profile, and is highly sensitive to the presence of active regions on the stellar photosphere.

To study the variability of the photospheric activity, we monitored the line profile variations of the CCF, in particular its contrast (CCFc) and full-width at half-maximum (FWHM), the Bisector Inverse Slope (BIS, Gray 2008) and the v_{asy} parameter (Figueira et al. 2013). We computed these indicators by means of custom made routines, developed by our team for HARPS-N spectra.

We also monitored the variability of the chromospheric activity. We focused on the Ca II H&K lines (3968.47 Å and 3933.66 Å respectively), the Na I D_{12} doublet (5889.95 Å and 5895.92 Å), the He I D_3 triplet (blend at 5875.62 Å), and the H_α line (6562.79 Å) as chromospheric diagnostics.

The analysis of the chromospheric indicators, that we will discuss in Sect. 6.1, is based on the differential comparison between the spectra in the series realigned in the wavelength space. This approach allows us to avoid the uncertainties related to the absolute flux calibration and continuum normalization, and is thus more robust than the one adopted by Scandariato et al. (2013), which depends on the normalization to the continuum (a difficult task in the presence of broad lines such as the Ca II H&K lines). Here we discuss how we reduced the data in order to perform the differential analysis, while in Sect. 6.1 we will analyse the variability in the spectra of τ Boo.

In the following analysis we excluded the data of night 4, because it has low S/N and no spectroscopic standard star was observed due to bad weather.

The Na I D_{12} doublet, the He I D_3 triplet and the H_α line are affected by telluric contamination, variable from night to night due to different airmasses and sky conditions. For each night of observation, the removal of telluric features from the target spectrum was performed via comparison with the spectrum of the standard star η UMa. Correction of telluric absorption was achieved using the task `telluric` in IRAF (Tody 1993). Conversely, the Ca II H&K spectral region of the standard star does not show any telluric feature above noise. Telluric correction was thus not performed on the corresponding spectral interval of τ Boo in order to preserve the original S/N.

In order to carry out the spectral differential analysis, we needed to rescale all the spectra to the same flux scale. To this purpose, we selected the spectrum at middle-time (i.e. the spectrum of night 6) with respect to which we performed the differential spectral analysis. This choice aims at minimizing any time-dependent instrumental effect along the time series of spectra (see below).

For each diagnostic, we extracted the corresponding spectral region, and we compared each spectrum in the series with the reference one on a pixel-by-pixel basis (Fig. 1), taking advantage of the wavelength stability of HARPS-N. In this way, the reference spectrum defined the common flux scale, and all the other spectra were rescaled accordingly using a linear best-fit of the flux vs. flux relation. The intercept adjusts the background level, while the slope rescales intrinsic stellar fluxes. Line cores were excluded from the best-fit to avoid any intrinsic non-linearity possibly introduced by chromospheric variability. The widths of the analysed spectral ranges and the line cores are reported in Table 3.

Table 3. Spectral ranges used for the analysed chromospheric diagnostics.

Line	Vacuum wavelength (Å)	Spectral width (Å)	Core width (Å)
Ca II K	3933.66	3.5	0.5
Ca II H	3968.47	3.5	0.5
Na I D_2	5889.95	3.5	0.3
Na I D_1	5895.92	3.5	0.3
He I D_3	5875.72	3.5	0.6
H_α	6562.79	3.5	0.5

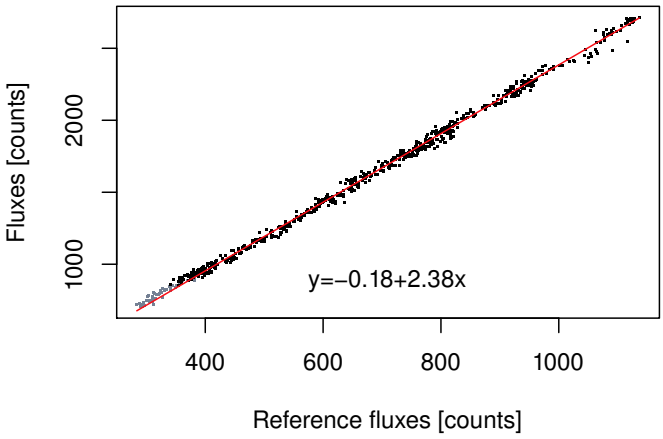

Figure 1. Example of the flux calibration of the mean spectrum of night 3 over the mean spectrum of night 6 in the Ca II K spectral range. The best fit (red line) is computed using the black dots, which represent instrumental fluxes out of the line core. The instrumental fluxes of the line core (in gray) are not included in the fit. The equation of the best fit is also shown.

This procedure generally led to satisfactory results, i.e. fluxes were well aligned along a straight line (Fig. 1). Still, in a few cases occurring especially with the Ca II K line, the residuals of the fit were larger than the noise up to ∼5% over small wavelength ranges, typically $\lesssim$1 Å (Fig. 2). These distortions, frequently observed during the first year of operation of HARPS-N, are not relevant in the measurement of RVs, but introduce spectral inhomogeneities on a night-to-night basis which may hamper the SPMI analysis. To correct for them, we divided the spectra by the reference one pixel by pixel, and we locally fitted the ratio with a low order polynomial, excluding a narrow window centered on the line cores where the SPMI signal may be mistaken as an instrumental effect. Finally, each spectrum was divided by the fitted ratio in order to remove the low order flux variations. In Fig. 2 we show an example of the low-order correction in the Ca II K line.

After the removal of distortions, we averaged the time series of the low-order corrected mean spectra for each spectral range. Then, for each mean spectrum we computed the relative residuals with respect to the averaged spectrum (Fig. 3), and integrated them over ∼1Å window around the line center, obtaining the Integrated Relative Deviation (IRD). The uncertainties on the IRDs are not easy to compute. As a matter of fact, the uncertainty introduced by the flux normalization depends on photon noise and the reduction inaccuracies, while the low-order correction tries to fix these inaccuracies, still with an uncertainty level depending on photon noise. We computed the uncertainties

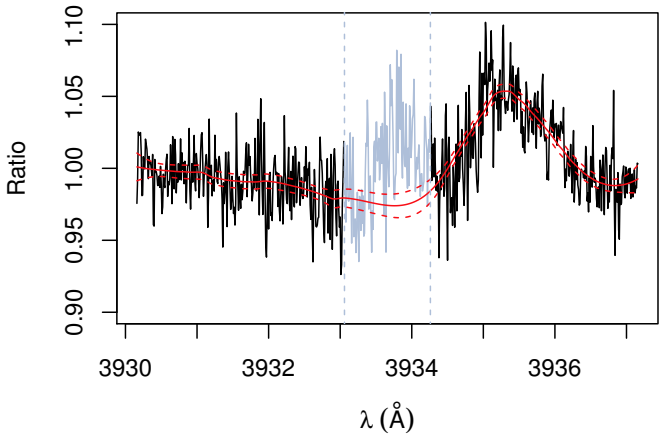

Figure 2. Example of the low-order correction of the Ca II K line. The black line is the ratio of one spectrum in the series to the reference spectrum, while the red line is the low order fit (95% confidence band is shown in red dashes). The vertical dashed lines bracket the line core, in gray, which is excluded from the fit.

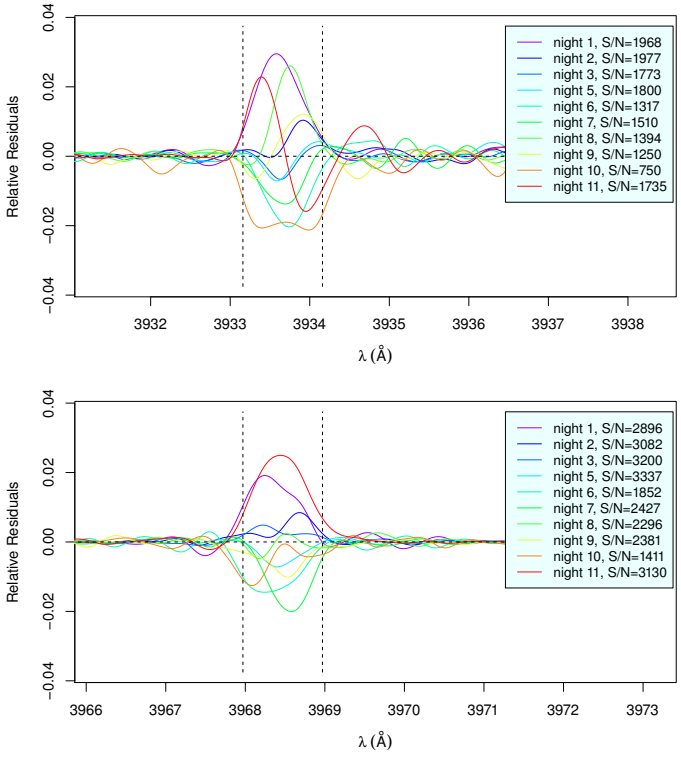

Figure 3. Residuals relative to the average spectrum of the Ca II K (top panel) and H (bottom panel) lines. The color code is reported in the legend, together with the S/N in the line for a 1 Å spectral element (night 4 has been excluded, see text). The residuals have been smoothed to avoid cluttering, for this reason they slightly exceed the vertical dashed lines.

on the IRDs by summing in quadrature photon noise and the uncertainties on flux calibration and low-order correction. In this way we are taking into account the same sources of error more than once, thus obtaining an upper limit to the true uncertainty.

The results of the whole procedure are presented in Sect. 6.

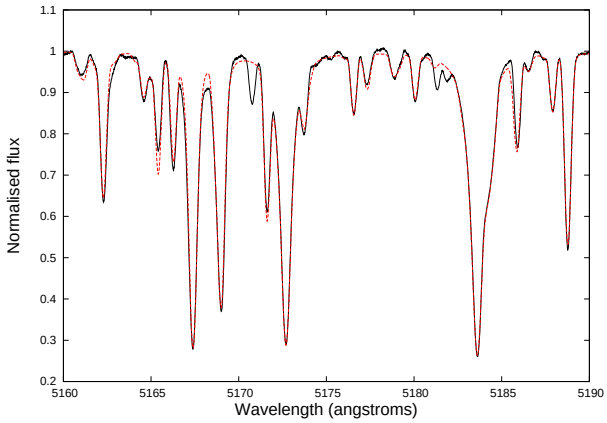

Figure 4. Fit of the observed mean spectrum (solid black line) with the synthetic one (dashed red line) in the wavelength region considered, using the SME software.

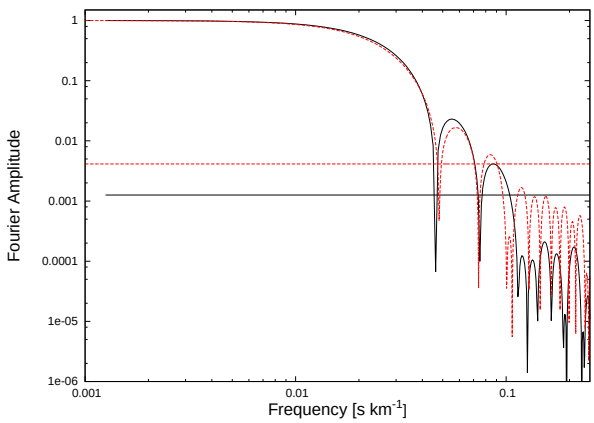

Figure 5. Amplitude of the Fourier transform of a mean line profile. Red dashed line refers to the LSD software, black solid line to the HARPS-N CCF. The horizontal lines show the noise level.

4. Stellar parameters

We derived the physical parameters of τ Boo by means of fitting synthetic spectra (ATLAS9 stellar atmosphere models, Castelli & Kurucz 2004) to a normalized HARPS-N mean file using the SME software by Valenti & Piskunov (1996). Unfortunately, the hydrogen lines could not be used to determine the temperature, because they span over several spectral orders, introducing problems in the normalization of the spectra. Therefore, we used the region between 5160 and 5190 Å, where the Mg triplet is found.

We computed the Vsin i using the Fourier transform of the CCF of a mean file (see Sect. 4.1). This value was kept fixed in the fit, while the other parameters were left free to vary. Table 4 shows our results, which are in good agreement with the values found in literature (e.g., Santos et al. 2013). A portion of the observed and synthetic spectra is shown in Fig. 4. An independent check of the stellar parameters was done with the method based on the equivalent widths of spectral absorption lines (Sousa et al. 2007; Biazzo et al. 2012, and references therein). Even if this method is not preferable due to the large Vsin i value of τ Boo, results were compatible with those estimated with the synthetic spectra method.

Table 4. Stellar parameters derived for τ Boo.

Parameter	Value
$T_{\rm eff}$ [K]	6399 ± 45
$\log g$ [cm s^{-1}]	4.27 ± 0.06
[Fe/H]	0.26 ± 0.03
Vsin i [km s^{-1}]	14.27 ± 0.06
Luminosity [$L_\odot$]	3.06 ± 0.16
Mass [$M_\odot$]	1.39 ± 0.25
Radius [$R_\odot$]	1.42 ± 0.08
$V_{\rm breakup}$ [km s^{-1}]	352 ± 67

We determined stellar radius and mass (Table 4) by combining the spectroscopic results with the parallax (64.03 ± 0.19 mas, van Leeuwen 2007) and using a bolometric correction (−0.0078, Torres 2010; Flower 1996).

4.1. Differential rotation

Using HARPS-N data, we found evidence of solar-like differential rotation in τ Boo by studying the Fourier transform of the mean line profiles of the mean spectra. We used two different mean line profiles: the CCF computed by the HARPS-N pipeline, and the profile obtained by using the LSD software (Donati et al. 1997) on the wavelength regions 4415-4805, 4915-5285, 5365-6505 Å. The CCF was computed using the Yabi interface, which means that we were able to reduce the spectra with our custom mask and further increasing the CCF half-window width up to 40 km s^{-1}, to insure having the whole mean line profile and the continuum.

We Fourier transformed both the LSD and the CCF profiles (Fig. 5) and found the values of the first two zero positions q_1 and q_2. The q_1 position gives an estimate of the projected rotational velocity Vsin i, while the ratio q_2/q_1 is an indicator of differential rotation (Reiners & Schmitt 2002), either solar-like ($q_2/q_1 < 1.72$) or anti-solar ($q_2/q_1 > 1.83$). We found $q_2/q_1 = 1.53 \pm 0.08$ for the LSD profile and $q_2/q_1 = 1.63 \pm 0.04$ for the CCF. The larger error in the LSD profile arises probably from the fact that we did not use the whole spectral range. These values are compatible with the results from Reiners (2006) ($q_2/q_1 = 1.57 \pm 0.04$) and Catala et al. (2007) ($q_2/q_1 = 1.60 \pm 0.02$).

The q_2/q_1 found can indicate either solar-like differential rotation (equator rotating faster than the poles) or strong gravity darkening in a rigidly rotating star. In the second case, the following empirical equation (Reiners 2003) can be used to infer the rotational velocity of the star:

$$q_2/q_1 = 1.75 + av + bv^2 \quad (1)$$

where a and b are parameters depending on the stellar spectral type. In particular, these parameters are $a = 0.172 \times 10^{-3}$ and $b = -0.993 \times 10^{-6}$ for F0 stars and $a = 0.184 \times 10^{-3}$ and $b = -0.116 \times 10^{-5}$ for G0 stars. τ Boo is classified as an F6 star, falling in the middle of these values, which means that in order to justify the values of q_2/q_1 found by means of rigid rotation the star rotational velocity should be either between 415 and 450 km s^{-1}(in the CCF case) or between 520 and 550 km s^{-1}(in the LSD case). Considering the values of mass and radius of Table 4, we can compute the breakup velocity $v_{\rm breakup} = 352$ km s^{-1}. For the values q_2/q_1 to be caused by gravity darkening the star

should rotate faster than the breakup velocity. We can then reliably estabilish that both the q_2/q_1 values found show the presence of solar-like differential rotation in τ Boo.

Adopting an inclination angle for the star $i = 40°$ (Donati et al. 2008) and using the q_2/q_1 values found, we can compute the differential rotation parameter $\alpha = \frac{\Delta\Omega}{\Omega_0}$, where Ω_0 is the equatorial angular velocity of the star, and $\Delta\Omega$ is the difference between the equatorial and polar angular velocities. Using the empirical relation (Reiners & Schmitt 2003):

$$\frac{\alpha}{\sqrt{\sin i}} = 2.74 - 5.16\left(\frac{q_2}{q_1}\right) + 4.32\left(\frac{q_2}{q_1}\right)^2 - 1.30\left(\frac{q_2}{q_1}\right)^3 \quad (2)$$

we found $\alpha = 0.24 \pm 0.07$ from $q_2/q_1 = 1.53$ (LSD profile) and $\alpha = 0.16 \pm 0.04$ from $q_2/q_1 = 1.63$ (CCF), both compatible with the value $\alpha = 0.18$ found by Catala et al. (2007). The LSD result is exactly the same of the differential rotation found by Donati et al. (2008) using spectropolarimetric measures.

Our work shows that the LSD profile and the CCF provide comparable values of q_2/q_1. As such, the CCF computed internally by the HARPS-N pipeline can be used as an indicator of differential rotation, at least in the case of high S/N spectra.

5. Orbital fit

For the nights where multiple HARPS-N exposures were taken, we used in the orbital fit the RV values obtained from the mean spectra (Table 2), in order to be independent from stellar oscillations. In addition to our HARPS-N data, we used the recently released archival data of Lick Observatory (Fischer et al. 2014). These data were obtained with 4 different Iodine-cell setups (identified as number 2, 13, 6, 8 in Table 5), that were taken in consideration during the analysis adding a RV shift as a free parameter to each set. We excluded all the data with $\sigma > 30$ m s^{-1}(e.g., all the data of the Lick setup number 2) and those that were not keeping the same instrumental setup continuously. The number of Lick RV measurements used in the orbital fit is 166. By combining Lick and HARPS-N data we obtained a dataset composed of 186 measurements, spanning a time interval of about 20 years.

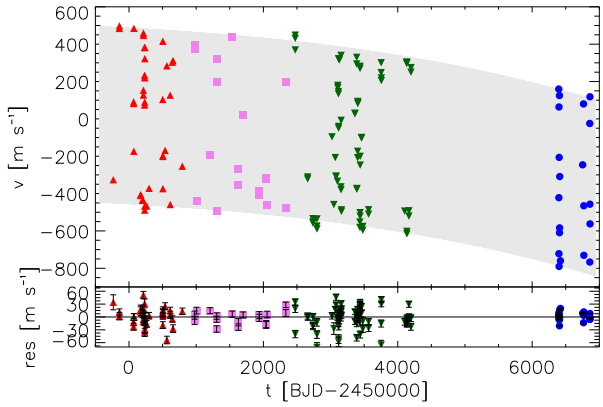

Figure 6. Two-objects orbital fit (gray) for the Lick Observatory archival data (red upward triangles, pink squares, green downward triangles corresponding to the different setup configurations 13, 6, 8 respectively) and HARPS-N data (blue circles). RV residuals are shown in the bottom plot.

We fitted the RVs with a Levenberg-Marquardt algorithm (Wright & Howard 2009), using a 2-planet model (Fig. 6) to take into account both the short-term variability due to the known planet and the long term trend due to the stellar binary companion (Sect. 5.1). To estimate the error-bars, we used a bootstrapping code (Wang et al. 2012). The orbital parameters obtained are reported in Table 5.

Table 5. Orbital parameters for the τ Boo system. Period and periastron of the binary companion τ Boo B were fixed to those of the Drummond (2014) astrometric solution.

Parameter	Value
τ Boo b	
Period [days]	$3.3124568 \pm 6.9 \times 10^{-6}$
$T_{periastron}$ [BJD_{UTC}-2450000]	6400.94 ± 0.30
K [m s^{-1}]	471.73 ± 2.97
e	0.011 ± 0.006
ω [deg]	113.4 ± 32.2
γ [m s^{-1}]	0.0
$m \sin i$ [M_{Jup}]	4.32 ± 0.04
semi-major axis [AU]	0.049 ± 0.003
τ Boo B	
Period [years]	964 ($fixed$)
$T_{periastron}$ [BJD_{UTC}-2450000]	12670 ($fixed$)
K [m s^{-1}]	1217.06 ± 222.36
e	0.71 ± 0.22
ω [deg]	94.1 ± 64.0
γ [m s^{-1}]	-1099.5 ± 273.0
$m \sin i$ [$M_\odot$]	0.4 ± 0.1
semi-major axis [AU]	109 ± 7
$offset_{Lick,setup13}$ [m s^{-1}]	0.0
$offset_{Lick,setup6}$ [m s^{-1}]	−23.17
$offset_{Lick,setup8}$ [m s^{-1}]	19.03
$offset_{HARPS-N}$ [m s^{-1}]	−16294.87
independent long term trends	
RV $slope_{Lick,setup2}$ [m s^{-1} y^{-1}]	2.7 ± 5.5
RV $slope_{Lick,setup13}$ [m s^{-1} y^{-1}]	-13.8 ± 5.6
RV $slope_{Lick,setup6}$ [m s^{-1} y^{-1}]	-8.8 ± 3.4
RV $slope_{Lick,setup8}$ [m s^{-1} y^{-1}]	-18.6 ± 2.4
RV $slope_{HARPS-N}$ [m s^{-1} y^{-1}]	-36.6 ± 4.0

We analysed in frequency the RV residuals shown in the bottom panel of Fig. 6, without finding any trace of additional periodicity. We note in particular that RV residuals of HARPS-N show a clear correlation with the pipeline-estimated bisector span (Fig. 7), supporting their stellar activity nature (discussed later in Sect. 6).

5.1. Stellar companion

Many astrometric measurements have been done to estimate the orbital parameters of the binary stellar system, with the most recent solutions (Roberts et al. 2011; Drummond 2014) claiming that the binary companion has a period < 1000 years, and will approach periastron within the next two decades.

To check if the RV data well match the astrometric best-fit orbit, we treated each Lick instrumental setup and HARPS-N separately. We fitted a 1-planet model, imposing the orbital solution for τ Boo b fixed, and keeping a long-term linear trend free (lower part of Table 5). In this way, we could put in evidence for

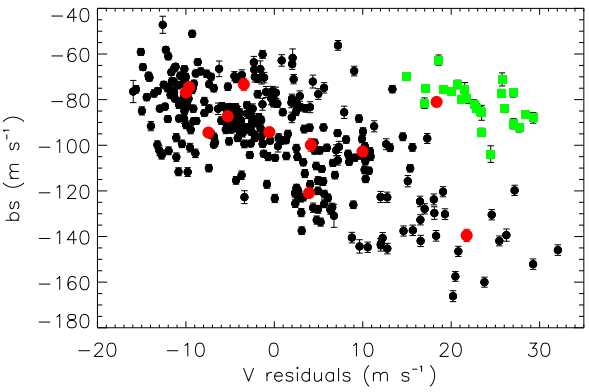

Figure 7. Residuals of the planetary fit for the HARPS-N measurements vs. the pipeline-estimated bisector span. The green squares refer to exposures taken at JD 2456421, during which the target was observed between clouds. Red circles are the measurements for the mean files. Error-bars for the bisector span are taken as twice the RV error.

the first time the changing of the slope in RVs caused by the binary companion τ Boo B. The information of the astrometric orbital parameters (Drummond 2014) and parallax (van Leeuwen 2007) imply a mass sum of $1.8 M_{\odot}$, and a value of $0.4 M_{\odot}$ for τ Boo B. We used this value to calculate the astrometric-based orbital RV slope caused on τ Boo A by the stellar companion (Fig. 8).

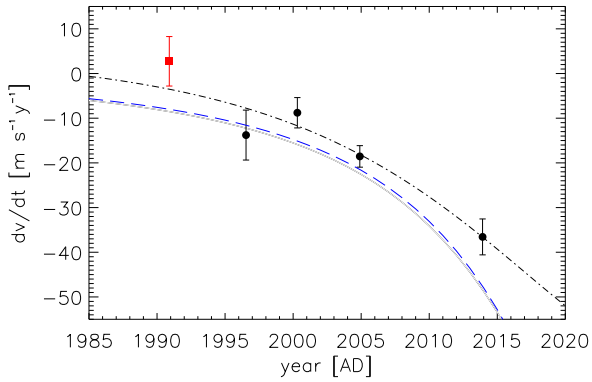

Figure 8. Points represent the values for the long-term RV slopes fitted on Lick and HARPS-N data. Red square is the fit on the first Lick setup with large error-bars, not taken in consideration for the fit of the planetary parameters. Black dot-dashed line represents the fitted orbit of the binary companion from the 2-objects fit of Table 5. Blue dashed line is the long term slope for the Drummond (2014) estimated best-fit orbit for the stellar binary companion, assuming a mass value of 0.4 $M_{\odot}$.

Clearly the data are not sufficient to give more constraints, but we can say that the best-fit astrometric solution is in good agreement with the present data. The fact that the slope calculated on HARPS-N data is more than twice those calculated on Lick data demonstrates that the star is rapidly accelerating due to the approaching of the periastron. A monitoring of the RV trend during the next years will give the possibility to obtain more reliable orbital parameters for the stellar binary companion.

6. Stellar activity

In this Section we aim to study the SPMI in the τ Boo system. To this purpose, we extensively analyse and compare all the magnetic activity indicators available, both computed directly from the spectra and extracted from the CCF (see Sect. 3).

6.1. Analysis of the IRD vs. IRD relationships

6.1.1. Ca II H&K and H_{α}

Figure 3 shows that the cores of the Ca II H&K lines are affected by variability larger than noise in the corresponding spectral regions. In Fig. 9 (left panel) we plot the corresponding IRDs of the two lines (IRD_H and IRD_K, respectively): we found that the two proxies are strongly correlated with each other with a confidence level of ~94%, thus validating the fact that the detected signal is not an artifact produced by our data reduction, but arises from the magnetic activity of the star. The significance of the correlation was computed by 10,000 random permutations of the data, which were also randomly perturbed by the corresponding uncertainties. Since the uncertainties on the variables are comparable, the best-fit line was computed by means of Ranged Major Axis (RMA) regression (Legendre & Legendre 1983).

Since the two H and K proxies are strongly correlated, we averaged them in order to obtain the collective IRD_{HK}. We found that the latter strongly correlates with the canonical $\log R'_{HK}$ (Noyes et al. 1984) computed following Lovis et al. (2011) (Fig. 9, middle panel).

Moreover, as shown in Fig. 9 (right panel), IRD_{HK} also strongly correlates with $IRD_{H_{\alpha}}$. A similar result was obtained by Fares et al. (2009), who spectroscopically monitored the activity level of τ Boo in 2008. This is consistent with different studies by other authors (Meunier & Delfosse 2009; Martínez-Arnáiz et al. 2010, 2011; Stelzer et al. 2013; Gomes da Silva et al. 2014), who found strong pairwise correlations between the H&K and the H_{α} lines despite the different formation heights (lower and upper chromosphere respectively), adopting different approaches (e.g., single-epoch comparison of many stars, multi-epoch variability study of single objects, emission line fluxes vs indices as relative measures).

6.1.2. Na I $D_{1,2}$ doublet and He I D_3 triplet

We found that the IRDs of the Na I D_1 and Na I D_2 lines linearly correlate, but with a confidence level not better than ~92% (Fig. 10, left panel). We carefully checked the spectra and we did not find any hint of bad telluric correction nor uncorrected terrestrial emission lines above the noise level. As described above for the H&K lines, we averaged the two proxies obtaining the IRD_{D12} indicator.

Plotting IRD_{D12} against IRD_{HK} (Fig. 10, middle panel), we did not find any correlation. This is consistent with the results of Díaz et al. (2007), who found a good correlation between the Na and Ca doublets only for stars with Balmer lines in emission (not the case of τ Boo). In any case, it is interesting to note that there is a bifurcation in the sample of measurements (Fig. 10, middle panel).

In a similar way, the IRD_{D12} vs IRD_{D3} plot seems to cluster into two subgroups (Fig. 10, right panel). The origin of the two trends is still unclear. Landman (1981), analysing a few quiescent prominences on the Sun, obtained a similar bifurcation comparing the intensities of the He I D_3 triplet with both Na I D_1 and D_2 lines. They conjectured, with no clear demonstration,

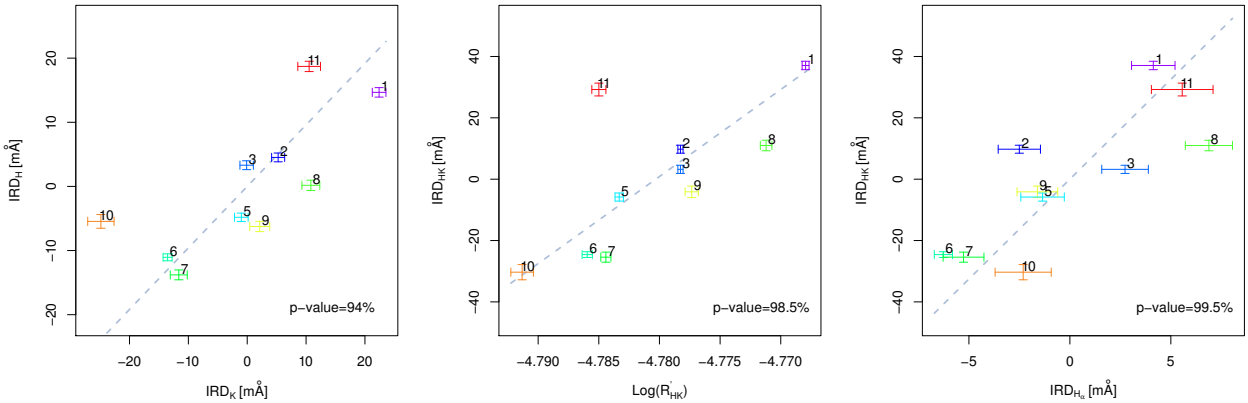

Figure 9. *Left panel:* IRD_H vs IRD_K. *Middle panel:* IRD_{HK} vs $Log(R'_{HK})$. *Right panel:* IRD_{HK} vs IRD_{H_α}. In all panels, the color code is the same as in Fig. 3, while the number in the bottom is the confidence returned by the correlation test. Numbers overplotted to data points indicate the ordered sequence in the series of observations. Gray dashes show the RMA best-fit.

that since the He triplet is back-heated by coronal UV radiation, then the two branches reflect the association of prominences with nearby coronal activity of different levels. The author remarks that the origin of the two branches is related to the He I D_3 triplet, as it shows the same bifurcation when compared to the intensity of the Ca II λ8498 line, while the latter well correlates with the Na I D_{12} lines. On the contrary, we found the bifurcation when IRD_{D12} is compared with both IRD_{D3} and IRD_{HK}, while there is no bifurcation in the IRD_{D3} vs. IRD_{HK} plot. Thus our results indicate that the formation of the Na I doublet should be investigated to explain this twofold behaviour.

Another possibility is the presence of prominence-like structures around the stars, formed with matter evaporating from the planet and supported by the magnetic field of the star (Lanza 2014). Since exoplanets are expected to be richer in metal than stars (e.g. Fortney et al. 2006), this may explain why the Na I shows the two branches instead of the He I D_3 triplet.

Focusing on the He I D_3 triplet, we found that the scatter of the IRD_{D3} measurements is slightly larger than uncertainties, indicating that weak variability in this proxy has occurred, if any. Moreover, we did not find the correlation with the Ca II H&K lines which has been previously found by Garcia-Lopez et al. (1993) in their sample of F-type main sequence stars. This is likely due to the fact that their statistical sample spans a large range of $\log R'_{HK}$, while τ Boo's chromospheric variability remained too limited during our observational campaign to detect such a correlation.

6.1.3. Parameters of the CCF

The very high S/N of the mean spectra allowed us to study in detail the CCF's variability to a large degree of accuracy. In particular, since the CCF is obtained from a large set of photospheric lines, the CCF's variability is indicative of the source and level of photospheric activity. It is thus interesting to study the CCF profile in order to understand the phenomenology of magnetism on the surface of τ Boo and how it is related to chromospheric activity.

As suggested by Nardetto et al. (2006), one way to analyse the CCF profile is to retrieve its width and contrast to the continuum by means of a gaussian best-fit. They also introduce the possibility to fit asymmetric profiles by tweaking the gaussian model. In the case of τ Boo, both methods leaded to poor fits of the observed CCF profiles, likely due to the fact that the differential rotation combined to the rotation rate of the star broadens the line profile in a non-gaussian way.

We thus approached the CCF profile analysis by averaging the CCFs returned by the DRS from the series of 10 nightly-averaged spectra, obtaining a master CCF profile with S/N higher then each nightly-averaged CCF's S/N. Then, we fit each nightly-averaged CCF with the master CCF allowing for changes in FWHM and contrast (CCFc).

We also computed the BIS and the v_{asy} parameter defined by Figueira et al. (2013). The former measures the velocity difference between the midpoints at the top and the bottom of the CCF (Gray 2008), while the latter gives an estimate of the asymmetry of the CCF profile. By definition, the computation of both parameters is model independent.

Since Queloz et al. (2001), variations in BIS are the paradigm for the signature of activity-induced RV variations. As a matter of fact, they found strong anti-correlation between the measured RVs and the corresponding BIS of the CCF. Since then, the anti-correlation between BIS and residual radial velocities (RV_{res}, the RVs minus the planetary orbit best fit) is considered a clear signature of short-term (i.e. rotationally induced) photospheric variability. In our case, BIS shows high degree of anti-correlation with the residual RV_{res} (Fig. 7). This suggests that RV_{res} are due to stellar activity.

Another couple of parameters showing strong anti-correlation is CCFc and FWHM (Fig. 11, left panel). This is consistent with the fact that while FWHM measures the width of the CCF at half maximum, CCFc counteracts in order to preserve the area of the CCF. The two indices are thus sensitive to the broadening of the wings of the CCF. We thus infer that correlations between these indices suggest broadening variability of the CCF.

Our results thus indicate that BIS follows the deformations of the CCF better than CCFc and FWHM which, in turn, are sensitive to the overall width of the CCF. BIS and CCFc can then be considered the best representatives of two different families of indicators. Given the operational definitions of BIS and CCFc, we can regard the former as an indicator of the mean distortion of line profile and the latter as an indicator of the mean strength of photospheric lines.

The weak variability of BIS with respect to measurement uncertainties compared to CCFc (Fig. 11, middle panel) may give some clues on the geometry of active regions on the stellar surface. As a matter of fact, the stability of BIS and the variability

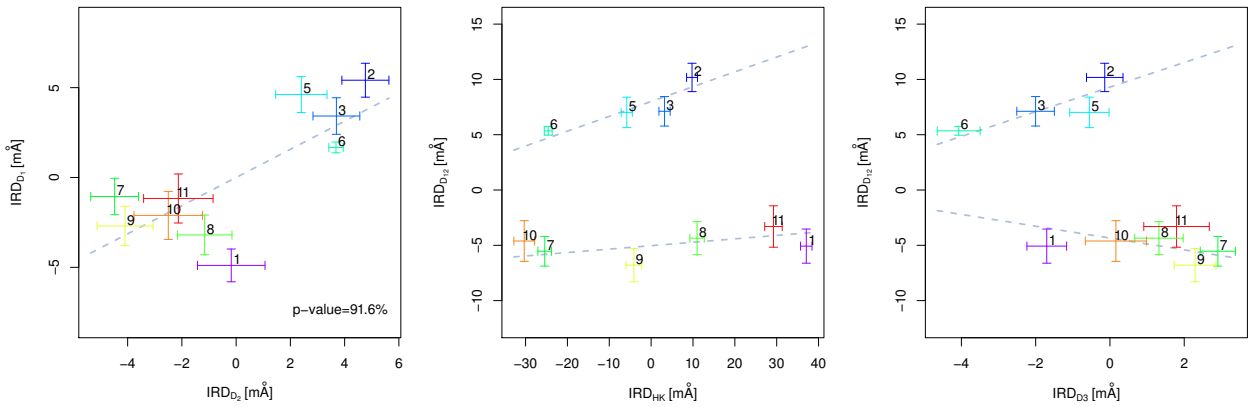

Figure 10. *Left panel:* IRD$_{D_1}$ vs IRD$_{D_2}$. *Middle panel:* IRD$_{D12}$ vs IRD$_{HK}$. *Right panel:* IRD$_{D12}$ vs IRD$_{D3}$. In all panels, the color code is the same as in Fig. 3 and represents different dates of observations. Numbers overplotted to data points indicate the ordered sequence in the series of observations. In the left panel, the number in the bottom is the confidence returned by the correlation test. In the middle and right panels, the two dashed gray lines are drawn by hand to highlight the bifurcation discussed in the text.

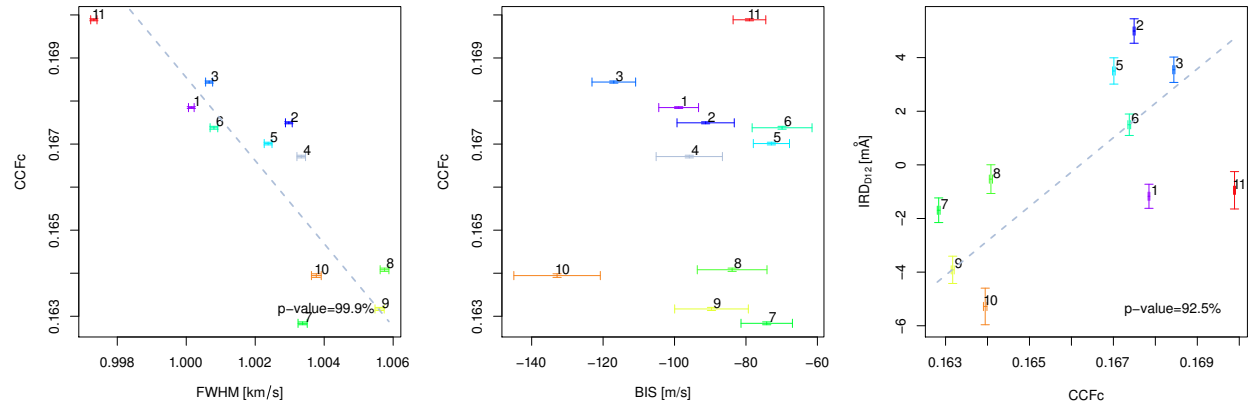

Figure 11. *Left panel:* CCFc vs FWHM. *Middle panel:* CCFc vs BIS. *Right panel:* IRD$_{D12}$ vs CCFc. Symbols and colors are the same as in Fig. 3.

of CCFc may indicate that the CCF changes its contrast with respect to the continuum, while preserving its overall asymmetry. This is consistent with a scenario with an active region around the pole of the star, which is not Doppler-shifted by stellar rotation and rapidly evolves in terms of contrast to the quiet photosphere (either in temperature difference and/or coverage factor).

We do not find any significant correlation between v_{asy} and the other parameters of the CCF.

When comparing the CCF parameters with the chromospheric indicators discussed in this Section, we found the strongest correlation between IRD$_{D12}$ and CCFc (p=92.5%, right panel in Fig. 11). The same applies for IRD$_{HK}$ and IRD$_{H_\alpha}$ with a lower confidence level (p$\lesssim$90%). We infer that the variability of the Na I D$_{12}$ doublet arises from changes in the line formation physics at the photospheric level, rather than genuine chromospheric emission. As a matter of fact, the doublet is formed in the lower chromosphere (Tripicchio et al. 1997), and is thus more closely related to the magnetic activity of the lowest chromosphere and photosphere. Moreover, as stated above, the Na I D$_{12}$ doublet is a good proxy for chromospheric activity only for mid-to-late type stars with emission Balmer lines, which is not the case of τ Boo.

6.2. Time series analysis

Using the ephemeris of τ Boo b reported in Table 5, we looked for the eventual phasing of each of the indicators discussed so far with the orbital motion of the planet. The most convincing cases are the phase-folding of IRD$_{HK}$ and IRD$_{H_\alpha}$ shown in left and middle panel of Fig. 12, where we set the phase $\phi = 0$ at the planetary inferior conjunction. In these diagrams we overplot the weighted least-squares best fit of the form IRD=A$\cdot \sin 2\pi\phi$+B$\cdot \cos 2\pi\phi$+C, where ϕ is the orbital phase and A, B, C are the parameters to be fitted. We exclude JD 2456396 (i.e. night 1) from the fit because it is clearly an outlier. The coefficient of determination R^2 of both fits is ~50%, i.e. the model explains ~50% of the total variance of the sample. Moreover, the likelihood ratio test suggests that the sinusoidal fit is to be preferred with respect to the flat model with a relative likelihood close to 100%.

For all the other indicators, both chromospheric and CCF-related, we obtained lower R^2 coefficient, i.e. we found weaker or no evidence of such a phasing. Conversely, we found that CCFc, and IRD$_{D12}$ consequently, shows a clear trend with time (right panel in Fig. 12). If we interpret that CCFc anti-correlates with magnetic activity (either spot-like or plage-like, see Dumusque et al. 2014), then the decrease of CCFc between JD 2456402 and 2456407 suggests that τ Boo increased its activity level, and conversely it turned over towards a quieter configuration between JD 2456411 and 2456422.

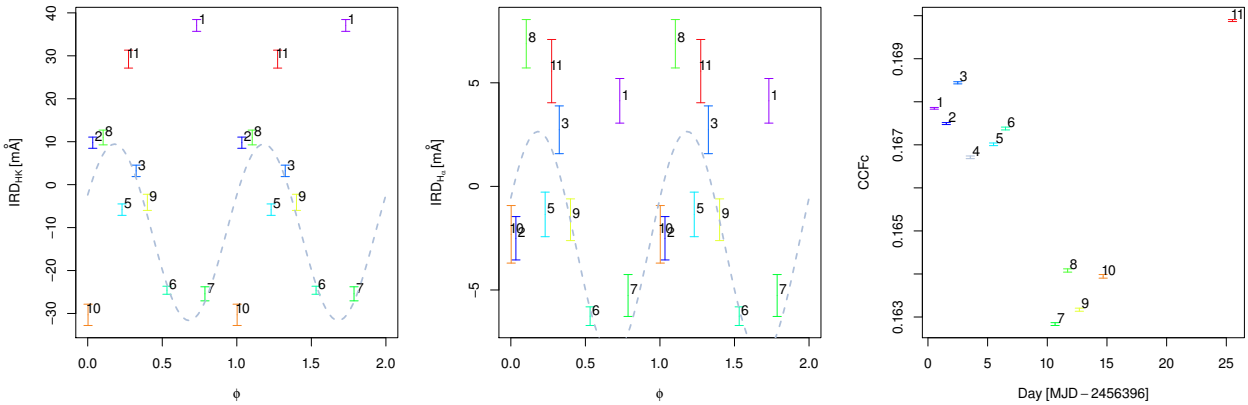

Figure 12. *Left panel:* Phase folded diagram of $\mathrm{IRD_{HK}}$. *Middle panel:* $\mathrm{IRD_{H_\alpha}}$. *Right panel:* Time series of the $\mathrm{CCFc}_{bigauss}$ measurements. The planetary inferior conjunction is at ϕ=0. Colors and numbers are the same as in the previous figures. In the left and middle panel, the gray dashed line is the least-squares best fit discussed in the text. We also report in the text the relative likelihood of the sinusoidal fit with respect to the flat model returned by the AICc.

6.3. Discussion

In Sect. 6.1 we argued that CCFc shows variations on time scales longer than the stellar rotation. Polar magnetic regions on τ Boo have already been detected in several epochs by Fares et al. (2013), who remark that the polarity of the magnetic field switches every ∼2 years. Moreover, inside each activity cycle they find signatures of rapid evolution of τ Boo's magnetic field. This supports the hypothesis that the variations of CCFc are driven by large scale evolution of magnetic activity, even along time spans as short as ∼20 days (Fig. 12, right panel).

Previous photometric monitoring of the star have never detected photometric variability above the mmag level (Baliunas et al. 1997; Walker et al. 2008). We thus assume that the typical peak-to-peak variability is of the order of 1 mmag as an upper limit. With this assumptions, and assuming that the active region is spot-dominated, using the SOAP2.0 code (Dumusque et al. 2014) we obtain that the active region covers ∼0.1% of the visible hemisphere. The corresponding peak-to-valley variations of RV, BIS and FWHM returned by the simulations are $\lesssim$25 m s^{-1}, while those of our measurements are actually larger (∼ 50 m s^{-1}, ∼70 m s^{-1}, ∼150 m s^{-1} respectively).

Conversely, if we assume that the active region consists of a bright plage, then the coverage factor is ≃2.5%. With this coverage, the simulated activity-induced signal in RV, BIS and FWHM is of the order of 100 m s^{-1}, comparable with those of our measurements. We thus conclude the high-latitude active region is likely to be plage-dominated.

In Sect. 6.2 we briefly discussed the time variability of the most representative indicators, finding that the genuine chromospheric ones, such as $\mathrm{IRD_{HK}}$ and $\mathrm{IRD_{H_\alpha}}$, seem to be phased with the orbital motion of the planet. This has been previously found by Walker et al. (2008), who detected a plage on τ Boo at planetary phase $\phi \simeq 0.8$ from Ca II H&K spectra in 2001 to 2003, and claim a photospheric spot using MOST photometric data taken in 2004 and 2005. The authors state that the persistence of the active region at the same longitude is a strong indication that it is due to a magnetic link between the planet and the star. On the other hand, Mathur et al. (2014) have recently reported a few cases of bona-fide single F-type stars observed with *Kepler* with active longitudes persisting on the stellar surface for many stellar rotations.

Since τ Boo's rotation period equals the planetary period (with some degree of differential rotation, Fares et al. 2009), it is still unclear whether the phasing of chromospheric activity with the planet is due to SPMI or to an active region simply corotating. In any case, if the SPMI scenario is confirmed, we remark that in our observing season the plage is located at ϕ ∼0.1-0.2 (Fig. 12), indicating that the magnetic connection between planet and star, if present, has moved between years 2005 and 2013. This may be due to a poloidal reversal of τ Boo's magnetic fields between these epochs. However, we remark that at phase 0.8 we find the largest scatter in the activity diagnostics: we have only two observations, and no statistical significance of this hypothesis can be assessed.

7. Asteroseismology

We have shown in the previous sections how the mean spectra could be used to get very precise radial velocity measurements to study the planetary and binary orbits and very accurate indicators to monitor the stellar activity and the star-planet interaction. We now describe the results obtained from the analysis of the high-cadence, short-exposure HARPS-N spectra.

We started our asteroseismic analysis with the correction of the Doppler shift due to the orbital motion of the planet (Sect. 5). Then, to remove the residual low-frequency term left in the data, several approaches were tried and we report here about the most powerful one, i.e., the subtraction of a linear trend from the data of each night. This procedure ensured us that no spurious low-frequency term (due to instrumental problems, planetary and binary orbits, RV variations induced by activity phenomena with timescales longer than the duration of one observing sequence) affects the radial velocity measurements used for the asteroseismic analysis.

This procedure returned timeseries centered at RV=0.0 m s^{-1} on each night (Fig. 13). The resulting RV curves show sporadic peak-to-peak variations up to 15 m s^{-1} (JD 2456399 and 2456410), but usually τ Boo is much more quiet, below 10 m s^{-1}. This amplitude is larger than that of the solar twin 18 Sco (Bazot et al. 2012), but comparable with that of the subgiant β Hyi (Bedding et al. 2007).

The timeseries were then analyzed in frequency to detect short-scale periodicities. We used the iterative sine-wave least-squares method (Vaníček 1971) and we checked the results with the Generalized Lomb-Scargle periodogram (Zechmeister & Kurster 2009). The power spectra are very similar and strongly

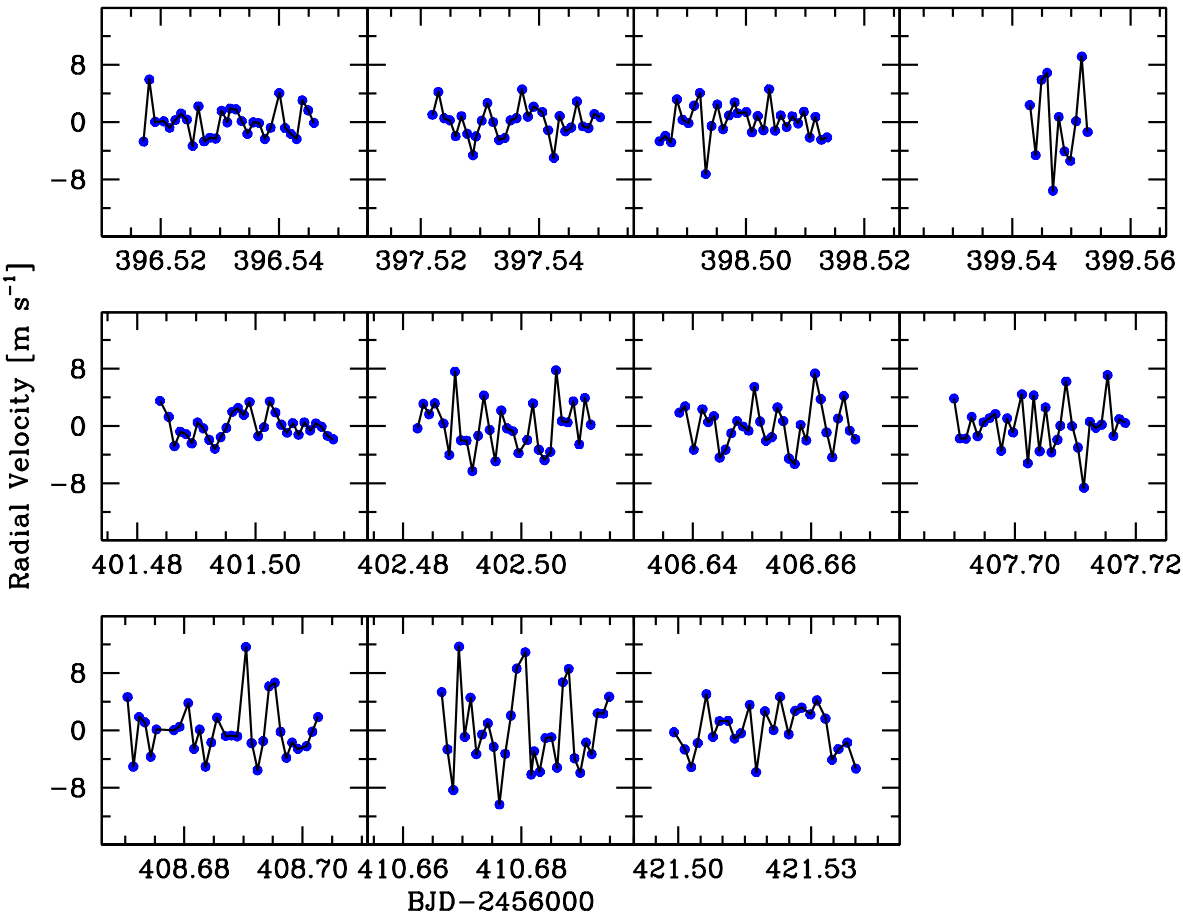

Figure 13. Asteroseismology of τ Boo: a linear fit was subtracted from the original HARPS-N data after the detrending from the planetary and binary orbits.

affected by the sampling of the observations. The spectral window shows strong aliases at multiples of 1 d^{-1}, i.e., 11.57 μHz (Fig. 14, insert in the top panel).

As expected from the limited time coverage, the frequency analysis of the RV values cannot supply an univoque determination of the asteroseismic content. The power spectrum is very noisy: a first relevant pattern occurs between 1.5 and 1.8 mHz, followed by another between 2.4 and 2.9 mHz (middle panel). Both are affected by the spectral window effects: each pulsational mode of τ Boo originates a structure similar to the spectral window, destroying the expected comb structure of the excited modes. The former pattern stands out a little more clearly over the noise and it shows the highest peaks around 1.68 mHz (bottom panel). The corresponding period of 9.9 min can be glimpsed in Fig. 13: it is traced by six consecutive measurements (60 sec exposure time, 25-35 sec overhead), but of course often modified by the interference with the other modes. The amplitudes of the peaks are very small, around 1.1 m s^{-1}. This value takes into account the intrinsic incoherence (amplitude damping, mode lifetimes) of the solar-like oscillations. We also calculated the level of the noise in the RV timeseries obtaining 0.35 m s^{-1}. The corresponding S/N=3.1 leaves some uncertainties on the significance of the 1.5-1.8 mHz pattern since the threshold S/N=4.0 (e.g., Bedding et al. 2007) was not reached. All these observational uncertainties are due to the limited time coverage: the doubling of the number of the measurements would have allowed us to reach the S/N=4.0 threshold.

7.1. The asteroseismic results: observation vs theory

The availability of a small set of high-precision radial velocity measurements allowed us to obtain an estimate of the asteroseismic parameters of τ Boo making a very limited observational investment. It is worthy to verify these results in a theoretical context.

We computed where the excess of power is expected in a star like τ Boo. To do that we used the scaling relations between stellar parameters (M, $T_{\rm eff}$, and L; Table 1) and the frequency of maximum power of the oscillations $\nu_{\rm max}$ (e.g., Stello et al. 2009). We obtained 1.98±0.46 mHz, compatible at $\pm1\sigma$ level with the observed value. We performed a further check on the detection of $\nu_{\rm max}$ by computing the power spectrum of the power spectrum to identify regularities in the detected frequencies. The most relevant feature was the 11.57 μHz spacing due to the aliasing effect. After this a peak at 94.4 μHz has appeared (insert in the bottom panel of Fig. 14). If the structure centered at 1.68 mHz is due to solar-like oscillations, then the 94.4 μHz spacing should be the large separation. Actually, the couple ($\nu_{\rm max}$, $\Delta\nu$)=(1680, 94) μHz matches the observed relation (see Fig. 2 in Stello et al. 2009). Though not yet decisive, these results are giving us more confidence in the asteroseismic approach to study the stars

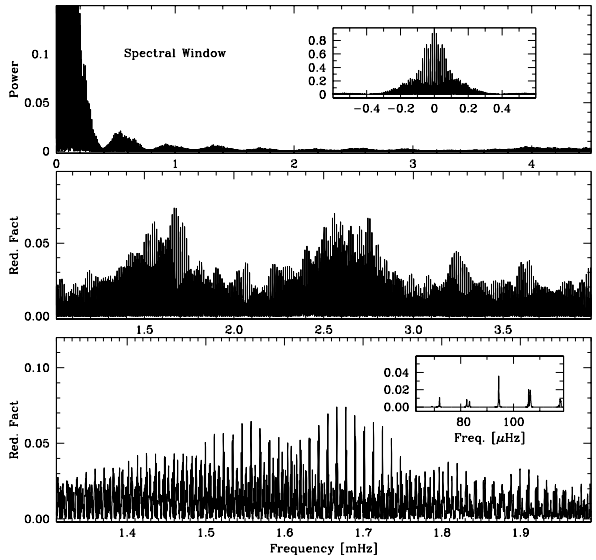

Figure 14. Asteroseismology of τ Boo. *Top panel*: spectral window of the HARPS-N data in the 0.0-4.5 mHz range and zoom in the 0.0-0.5 mHz range (insert). *Middle panel*: power spectrum in the 1.0-4.0 mHz range. *Bottom panel*: power spectrum in 1.3-2.0 mHz range and power spectrum of this spectrum (insert).

hosting exoplanets by means of radial velocity measurements performed mainly for other purposes.

8. Evolutionary stage

It has been well demonstrated (e.g., Cunha et al. 2007) that accurate determination of mass and radius combined with the spectroscopic measurements of atmospheric parameters allows us to well constrain stellar structure of observed stars.

Thus, in order to assess the information available from HARPS-N observations, we calculated a grid of theoretical structure models of τ Boo evolved from chemically uniform model on the zero-age main sequence, by using the ASTEC evolution code (Christensen-Dalsgaard 2008a) and by varying the mass and the composition in order to match the atmospheric parameters available (see Table 4).

The evolutionary models have been produced by employing up-to-date physical information by following the procedure described in Di Mauro et al. (2011). The input physics for the evolution calculations included the OPAL 2005 equation of state (Rogers & Nayvonov 2002), OPAL opacities (Iglesias & Rogers 1996), and the NACRE nuclear reaction rates (Angulo et al. 1999). Convection was treated according to the mixing-length formalism (MLT; Böhm-Vitense 1958) and defined through the parameter $\alpha = \ell/H_p$, where H_p is the pressure scale height. The initial heavy-element mass fraction Z_i has been calculated from the iron abundance given in Table 4 using the relation [Fe/H]= $\log(Z/X) - \log(Z/X)_\odot$, where (Z/X) is the value at the stellar surface. We obtained $Z/X = 0.045 \pm 0.003$ assuming the solar value $(Z/X)_\odot = 0.0245$ (Grevesse & Noels 1993).

The resulting evolutionary tracks are characterized by the input stellar mass M, the initial chemical composition and a mixing-length parameter.

The location of the star in the H-R diagram identifies τ Boo as being at the beginning of the main sequence phase of core hydrogen burning, with an internal content of hydrogen in the core of about $X_c = 0.5$. As predicted by Fares et al. (2009), it has a shallow convective region, with a depth of about $D_{cz} \simeq 0.1R$, typical of stars in this phase. According to the stellar evolution constraints, given the match with the observed atmospheric properties, and with the use of all the possible values of mass and metallicity, our computations show that the age of τ Boo is 0.9 ± 0.5 Gyr and the mass is $M = 1.38 \pm 0.05 M_\odot$. It is clear that the accuracy on the values of age and mass here inferred are dependent on the stellar model calculation procedure, and in particular on the physical and chemical inputs (e.g., Lebreton et al. 2014). Here we limit to notice that lower values of the solar heavy-element abundance $(Z/X)_\odot$ led to a mass lower by 5% and an age higher by 30%. These values are in agreement with those deduced above within 2-σ uncertainty limits. The Lithium line at 6708Å could not be used to confirm the young age, since $T_{\rm eff} = 6399K$ (Table 4) puts τ Boo in the Lithium dip (e.g., Balachandran 1995).

The value of age which has been obtained by direct modeling results to be better constrained than the large range of previous values obtained by different methods, like the empirical relation between large scale magnetic fluxes and age reported by Vidotto et al. (2014), chromospheric activity (Saffe et al. 2005; Henry et al. 2000), isochrone techniques (Saffe et al. 2005; Suchkov & Schultz 2001) or X-ray luminosity (Sanz-Forcada et al. 2010).

In order to reproduce the oscillation observations obtained in Sect. 7, among all the computed models we selected the ones which best fit the observations. For the selected models we calculated the adiabatic oscillation frequencies using the ADIPLS code (Christensen-Dalsgaard 2008b). According to our calculations this star should show solar-like pulsations with a spectrum in the interval $700 - 2600$ μHz and frequencies equally spaced by a large separation of about $\Delta\nu = 95 \pm 1$ μHz. The observed large separation appears in excellent agreement with the theoretical one. The range of frequencies is very similar, though the spectral window effects makes very difficult a straight comparison. We can conclude that there is no discrepancy between the values we could infer from the limited HARPS-N observations and the current modeling of solar-like oscillations in τ Boo.

8.1. Tidal evolution

Lanza (2010) and Damiani & Lanza (2015) found that the rotation period $P_{\rm rot}$ in a sample of main-sequence stars with $T_{\rm eff} \gtrsim 6300$ K accompanied by hot Jupiters with orbital period $P_{\rm orb}$ verifies the relationship $1 \geq P_{\rm rot}/P_{\rm orb} \geq 2$ (cf. Fig. 10 in Damiani & Lanza 2015). Given its almost synchronous rotation, τ Boo satisfies this relationship as well. The timescale of tidal synchronization of the stellar rotation is at least $1 - 2$ orders of magnitudes longer than the stellar age (e.g., Donati et al. 2008; Barker & Ogilvie 2009), suggesting that the system reached the ZAMS close to its current synchronous state. The subsequent evolution was characterized by a weak tidal interaction between the planet and the star with a very slow braking of the stellar rotation, owing to the low braking efficiency of the stellar winds of mid-F type stars (cf. Damiani & Lanza 2015, Sect. 6.1.2 for details). In other words, the present orbital and rotational angular momenta in the τ Boo system are likely to be close to the initial ones with very little evolution since the system arrived on the ZAMS.

9. Conclusions

We studied the τ Boo system by means of a new observational strategy applied to HARPS-N spectra collected in the framework of the GAPS project. It allowed us to obtain both high-cadence 60-sec exposures to monitor the solar-like oscillations and high S/N, non-saturated spectra to study stellar activity and star-planet interaction.

We developed new computational tools to perform the co-addition of consecutive spectra and subsequent average of them, preserving the correct computation of the BERV (and thus RV) values that have to be referred to the flux-balanced reference time. Implementing a custom mask for τ Boo allowed us to extract more accurate RV values; the adaptation of the Yabi platform gave us the possibility to test and verify these new tools in an user-friendly system.

Our results can be resumed in the following points.

- We updated the ephemeris for the planet τ Boo b and showed, by means of our RVs, that the binary companion τ Boo B is rapidly accelerating, confirming the astrometric predictions that it is approaching the periastron on a highly eccentric orbit. We plan to take additional observations in the next years to have a more reliable value of its eccentricity.
- The SME software was applied to determine new stellar parameters, giving the same results as the equivalent width method. In particular we refined the values of mass and radius to $1.39 \pm 0.25\,M_\odot$ and $1.42 \pm 0.08\,R_\odot$. We could establish that the star shows strong differential rotation, which we determined by means of both the LSD mean line profile and the CCF. We stress that the CCF computed by the HARPS-N pipeline can then be reliably used as an indicator of differential rotation.
- The analysis of the correlations between several indices pointed out evident chromospheric activity. In particular, the activity indicators extracted from HARPS-N spectra suggest the presence of a plage around one of the poles of the star. The nature of the chromospheric activity remains uncertain. It is unclear if it is due to SPMI or to a corotating active region, or both.
- Solar-like oscillations are detected in the RV timeseries. Though very limited by the spectral window, we could infer observational values of ν_{max} and $\Delta\nu$. These values are in good agreement both with the scaling relations and the asteroseismic model computed from our stellar parameters. This result supports our confidence in the application of the asteroseismic approach to other bright stars hosting exoplanets to constrain their ages and masses.
- From the evolutionary point of view, τ Boo is at the beginning of the main sequence phase of core hydrogen burning, with an age of 0.9 ± 0.5 Gyr. The model built allowed us to further constrain the value of the stellar mass to 1.38 ± 0.05 $M_\odot$ and thus, using $i = 44.5 \pm 1.5°$ (Brogi et al. 2012), the mass of the planet to $6.13 \pm 0.17\,M_{Jup}$.

Acknowledgements. The GAPS project acknowledges support from INAF through the "Progetti Premiali" funding scheme of the Italian Ministry of Education, University, and Research.

References

Angulo, C., Arnould, M., Rayet M., et al. 1999, Nucl. Phys. A, 656, 3
Balachandran, S. 1995, ApJ, 446, 203
Baliunas, S. L., Henry, G. W., Donahue, R. A., et al. 1997, ApJ, 474, L119
Barker, A. J., & Ogilvie, G. I. 2009, MNRAS, 395, 2268
Bazot, M., Ireland, M.J., Huber, D., et al. 2012, A&A,
Bedding, T.R., Kjeldsen, H., Arentoft, T., et al. 2007, ApJ, 663, 1315
Biazzo, K., D'Orazi, V., Desidera, S., et al. 2012, MNRAS, 427, 2905
Böhm-Vitense, E., 1958, Zeitschrift für Astrophysik, 46, 1115
Borsa, F. , Rainer, M., Poretti, E. 2013, Internal report GAPS-SCI-REP-006
Brogi, M., Snellen, I. A. G., de Kok, R. J., et al. 2012, Nature, 486, 502
Butler, R. P., Marcy, G. W., Williams, E., et al. 1997, ApJ, 474, L115
Butler, R. P., Wright, J. T., Marcy, G. W., et al. 2006, ApJ, 646, 505
Castelli, F., & Kurucz, R. L. 2004, arXiv:astro-ph/0405087
Catala, C., Donati, J.-F., Shkolnik, E., et al. 2007, MNRAS, 374, L42
Christensen-Dalsgaard, J. 2008a, Ap&SS, 316, 13
Christensen-Dalsgaard, J. 2008b, Ap&SS, 316, 113
Collier Cameron, A., Horne, K., Penny, A., & James, D. 1999, Nature, 402, 751
Cosentino, R., Lovis, C., Pepe, F., et al. 2012, Proc. SPIE, 8446,
Covino, E., Esposito, M., Barbieri, M., et al. 2013, A&A, 554, A28
Cunha, M. S., Aerts C., Christensen-Dalsgaard J. et al. A&ARv 14, 217
Damiani, C., & Lanza, A. F., 2015, A&A, 574, A39
Di Mauro, M. P., Cardini, D., Catanzaro, G. et al., 2011, MNRAS, 415, 3783
Díaz, R. F., Cincunegui, C., & Mauas, P. J. D. 2007, MNRAS, 378, 1007
Donati, J.-F., Moutou, C., Farès, R., et al. 2008, MNRAS, 385, 1179
Donati, J.-F., Semel, M., Carter, B. D., et al. 1997, MNRAS, 291, 658
Drummond, J. D. 2014, AJ, 147, 65
Dumusque, X., Boisse, I., & Santos, N. C. 2014, ApJ, 796, 132
Fares, R., Donati, J.-F., Moutou, C., et al. 2009, MNRAS, 398, 1383
Fares, R., Moutou, C., Donati, J.-F., et al. 2013, MNRAS, 435, 1451
Figueira, P., Santos, N. C., Pepe, F., et al. 2013, A&A, 557, AA93
Fischer, D. A., Marcy, G. W., & Spronck, J. F. P. 2014, ApJS, 210, 5
Flower, P. J. 1996, ApJ, 469, 355
Fortney, J. J., Saumon, D., Marley, M. S., et al. 2006, ApJ, 642, 495
Garcia-Lopez, R. J., Rebolo, R., Beckman, J. E., & McKeith, C. D. 1993, A&A, 273, 482
Gomes da Silva, J., Santos, N. C., Boisse, I., et al. 2014, A&A, 566, AA66
Gratton, R. 2013, Internal report GAPS-SCI-REP-002
Gray, D. F. 2008, The Observation and Analysis of Stellar Photospheres, by David F. Gray, Cambridge, UK: Cambridge University Press, 2008,
Grevesse, N. & Noels, A. 1993 in Origin and Evolution of the Elements, ed. S. Kubono & T. Kajino, 14
Henry, G. W., Baliunas, S. L., Donahue, R. A., et al. 2000, ApJ, 531, 415
Hunter A.A., Macgregor A.B., Szabo T.O., et al., Yabi: An online research environment for Grid, High Performance and Cloud computing, Source Code for Biology and Medicine 2012, 7:1
Iglesias, C. A., & Rogers F. J. 1996, ApJ, 464, 943
Landman, D. A. 1981, ApJ, 251, 768
Lanza, A. F. 2009, A&A, 505, 339
Lanza, A. F. 2010, A&A, 512, AA77
Lanza, A. F. 2012, A&A, 544, AA23
Lanza, A. F. 2014, A&A, 572, LL6
Lebreton, Y., Goupil, M. J., & Montalbán, J. 2014, EAS Publications Series, 65, 99
Legendre, P., Legendre, L., 1998, Numerical Ecology, Elsevier
Lockwood, A. C., Johnson, J. A., Bender, C. F., et al. 2014, ApJ, 783, L29
Lovis, C., Dumusque, X., Santos, N. C., et al. 2011, arXiv:1107.5325
Martínez-Arnáiz, R., Maldonado, J., Montes, D., et al. 2010, A&A, 520, AA79
Martínez-Arnáiz, R., López-Santiago, J., Crespo-Chacón, I., & Montes, D. 2011, MNRAS, 414, 2629
Mathur, S., García, R. A., Ballot, J., et al. 2014, A&A, 562, AA124
Meunier, N., & Delfosse, X. 2009, A&A, 501, 1103
Nardetto, N., Mourard, D., Kervella, P., et al. 2006, A&A, 453, 309
Noyes, R. W., Hartmann, L. W., Baliunas, S. L., et al. 1984, ApJ, 279, 763
Pepe, F., Mayor, M., Galland, F., et al. 2002, A&A, 388, 632
Queloz, D., Henry, G. W., Sivan, J. P., et al. 2001, A&A, 379, 279
Rainer, M. 2013, Internal report GAPS-SCI-REP-007
Reiners, A., & Schmitt, J. H. M. M. 2002, A&A, 384, 155
Reiners, A. 2003, A&A, 408, 707
Reiners, A., Schmitt, J.H.M.M., 2003, A&A, 398, 647
Reiners, A. 2006, A&A, 446, 267
Roberts, L. C., Jr., Turner, N. H., ten Brummelaar, T. A., et al. 2011, AJ, 142, 175
Rodler, F., Kürster, M., & Henning, T. 2010, A&A, 514, A23
Rodler, F., Lopez-Morales, M., & Ribas, I. 2012, ApJ, 753, L25
Rogers, F. J., Nayvonov, A. 2002, ApJ, 576, 1064
Saffe, C., Gómez, M., & Chavero, C. 2005, A&A, 443, 609
Santos, N.C., Israelian, G., Mayor, M., et al. 2004, A&A, 415, 1153
Santos, N. C., Sousa, S. G., Mortier, A., et al. 2013, A&A, 556, AA150
Sanz-Forcada, J., Ribas, I., Micela, G., et al. 2010, A&A, 511, LL8
Scandariato, G., Maggio, A., Lanza, A. F., et al. 2013, A&A, 552, AA7
Shkolnik, E., Walker, G. A. H., Bohlender, D. A., et al. 2005, ApJ, 622, 1075
Shkolnik, E., Bohlender, D. A., Walker, G. A. H., & Collier Cameron, A. 2008, ApJ, 676, 628

Sousa, S. G., Santos, N. C., Israelian, G., et al. 2007, A&A, 469, 783
Stello, D., Chaplin, W.J., Basu, S., Elsworth, Y., & Bedding, T.R. 2009, MNRAS,
Stelzer, B., Frasca, A., Alcalá, J. M., et al. 2013, A&A, 558, AA141
Suchkov, A. A., & Schultz, A. B. 2001, ApJ, 549, L237
Tody, D. 1993, Astronomical Data Analysis Software and Systems II, 52, 173
Torres, G. 2010, AJ, 140, 1158
Tripicchio, A., Severino, G., Covino, E., et al. 1997, A&A, 327, 681
Valenti, J.A., Piskunov. N.E. 1996, A&A, 118, 595
van Leeuwen, F. 2007, A&A, 474, 653
Vaniĉek, P. 1971, Ap&SS, 12, 10
Vidotto, A.A., Gregory, S.G., Jardine, M. et al., 2014, MNRAS, 441, 2361
Walker, G. A. H., Croll, B., Matthews, J. M., et al. 2008, A&A, 482, 691
Wang, X., Sharon, Wright, J. T., Cochran, W., et al. 2012, ApJ, 761, 46
Wright, J. T., & Howard, A. W. 2009, ApJS, 182, 205
Zechmeister, M., & Kürster, M. 2009, A&A, 496, 577